Chapter 4
Pathways and Interfaces Under Stress Redistribution

Markus Barsch, Thomas Nagel, Holger Steeb, Patrick Schmidt, Dongwon Lee, Carlos Guevara Morel, and Jobst Maßmann

There are several finite element-based modeling approaches to deal with fissures, fractures and discontinuities in rocks. A recent overview can found e.g in Mollaali et al. (2022). As one of them, lower-dimensional interface elements (LIE) were implemented in OpenGeoSys[1] previously (Watanabe et al. 2012; Yoshioka et al. 2019) to map fractures and fissures discretely.

For example, in a 3D model consisting of a matrix and a fracture, the matrix is represented by 3D elements and the fracture by 2D elements. Crack growth can occur along pre-defined interfaces, i.e. the 2D elements, and therefore, the direction of crack path is predefined in contrast to other approaches resting on phase fields, extended finite elements or remeshing strategies.

[1] https://www.opengeosys.org.

M. Barsch (✉) · T. Nagel
TUBAF, Technische Universität Bergakademie Freiberg, Freiberg, Germany
e-mail: Markus.Barsch1@ifgt.tu-freiberg.de

T. Nagel
e-mail: thomas.nagel@ifgt.tu-freiberg.de

H. Steeb · P. Schmidt · D. Lee
UoS, University of Stuttgart, Stuttgart, Germany
e-mail: holger.steeb@mechbau.uni-stuttgart.de

P. Schmidt
e-mail: patrick.schmidt@mechbau.uni-stuttgart.de

D. Lee
e-mail: dongwon.lee@mechbau.uni-stuttgart.de

C. Guevara Morel · J. Maßmann
BGR, Federal Institute for Geosciences and Natural Resources, Hanover, Germany
e-mail: Carlos.GuevaraMorel@bgr.de

J. Maßmann
e-mail: Jobst.Massmann@bgr.de

O. Kolditz et al. (eds.), *GeomInt—Discontinuities in Geosystems From Lab to Field Scale*, SpringerBriefs in Earth System Sciences,
https://doi.org/10.1007/978-3-031-26493-1_4

Further, lower-dimensional approaches taking into account the hydromechanics of deformable fluid-saturated fractures in porous media have been implemented in open-source software packages like DUNE[2] or FEniCS[3] (Schmidt and Steeb 2019; Schmidt et al. 2021). Numerically efficient coupling approaches for fractures and the surrounding porous rock allowing for HPC computations based on lower-dimensional models have been successfully applied to complex 2D/3D problems (Schmidt et al. 2022b) using modern code-coupling tools like preCICE.[4]

This general framework can be applied to a range of problems aside from fracture mechanics, including fracture slip problems and geotechnical problems with frictional interfaces, such as soil-structure interaction. In the sequel, we briefly summarize the theory and give a short insight into selected application examples from the GeomInt2 project. In cooperation with researchers from STIMTEC (Renner 2020) and others, those simulation tools have been used for the numerical interpretation of pressure transients obtained from large-scale experiments in the field, like e.g. harmonic pumping tests at the underground laboratory Reiche Zeche, Freiberg, Germany (Schmidt et al. 2021) or at the Grimsel Test Site, Switzerland, (Schmidt et al. 2022a). Based on those numerical-experimental investigations it was shown that fully-coupled hydromechanical approaches give a more physically sound insight into pressure transients especially if results are compared to simpler and more "classical" diffusion-based modeling approaches.

4.1 Hydro-Mechanics of Deformable High-Aspect Ratio Fractures

Viscous fluid flow in fractured porous rocks is causing strongly coupled hydro-mechanical interaction phenomena by local aperture, i.e. volume, changes of the fractures and resulting variations of the fluid pressure state. These phenomena have been investigated by various researchers over the last decades. For an overview we refer to a recent PhD thesis written during the period of the GeomInt and GeomInt2 project (Schmidt 2022).

Modelling approaches of fractured reservoirs require an efficient description of the hydro-mechanical processes. This includes on the one hand the accurate description of the deformation of the fracture and on the other hand the dynamic exchange of momentum between the fractures and the surrounding rock matrix. From a continuum perspective, model assumptions have to be made for the geometry of the fracture, and in a lower-dimensional setup, for the velocity profile within the fracture domain. For low Reynolds-number flow ($\mathrm{Re} < 1$), a hybrid-dimensional model approach is obtained by an integration of the assumed parabolic flow velocity profile in normal fracture direction $\hat{\mathbf{e}}_3$. This "a priori" integration is reducing the fracture flow domain

[2] https://www.dune-project.org.

[3] https://fenicsproject.org/.

[4] https://precice.org.

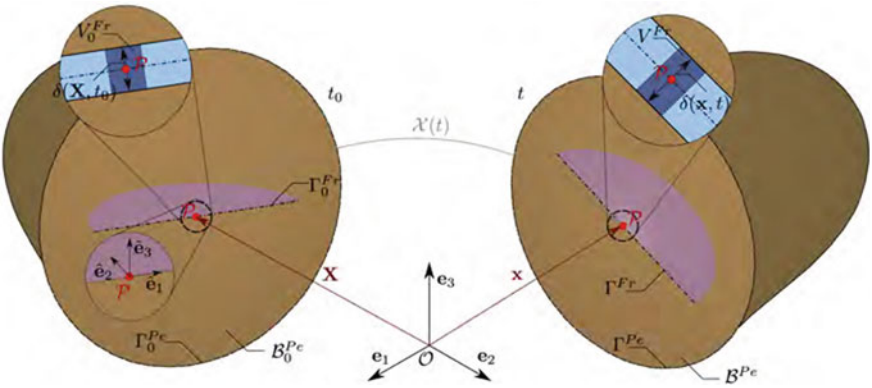

Fig. 4.1 Representation of a single fracture Γ_{Fr} embedded in a poro-elastic material body $\mathcal{B}^{Pe}$ with material surface Γ^{Pe}. For the kinematical description of the fracture, a local basis system $\hat{\mathbf{e}}_i$ is introduced. The basis vector $\hat{\mathbf{e}}_3$ is aligned with the fracture surface normal. The mechanical deformation of the fracture, and therefore the local volume change, is depicted with the evolution of the aperture δ, cf. Schmidt et al. (2022b), Schmidt (2022)

by one dimension, cf. Fig. 4.1. The resulting model is derived from 3D continuum mechanics by a consistent evaluation of the conservation of mass and balance of momentum under fully saturated conditions (Vinci et al. 2014; Schmidt 2022).

Without going into details of the derivations of models, we recapitulate here only the main governing equations. The bulk properties of the porous rock are described with the quasi-static linear poro-elastic equations (Biot 1941; Steeb and Renner 2019)

$$\begin{aligned} -\operatorname{div}\boldsymbol{\sigma} &= \rho\,\mathbf{b}, \\ \frac{1}{M}\frac{\partial p}{\partial t} - \frac{k^f}{\gamma_0^{fR}}\operatorname{div}\operatorname{grad} p &= -\alpha\,\operatorname{div}\frac{\partial \mathbf{u}_s}{\partial t}. \end{aligned} \tag{4.1}$$

In Eq. 4.1 we introduced the local storativity $1/M$ of the porous rock, Biot's coupling parameter α, the isotropic hydraulic conductivity k^f, and the effective weight of the fluid γ_0^{fR}. The total stresses are given by $\boldsymbol{\sigma}$, the pore pressure is denoted with p, body forces are introduced as $\rho\,\mathbf{b}$ and the displacements of the solid skeleton are given by $\mathbf{u}_s$. The set of coupled equations are supplemented with boundary conditions (Steeb and Renner 2019).

From first principles, a pressure diffusion equation could be derived for the evolution of the pressure state within the fracture. For high aspect ratio fractures, cf. Vinci et al. (2014), the final partial differential equation could be written in a simple non-linear format taking into account the evolution of aperture δ as well as fluid leak-off through an exchange term with the matrix $\hat{q}$ (normal component of the seepage velocity)

$$\frac{\partial \hat{p}}{\partial t} - \frac{\delta^2}{12\,\eta^{fR}\,\beta^f}\operatorname{div}\operatorname{grad}\hat{p} + \frac{1}{\delta\,\beta^f}\frac{\partial \delta}{\partial t} = \frac{\hat{q}}{\delta\,\beta^f}. \tag{4.2}$$

In Eq. 4.2, we have introduced fluid properties like the effective dynamic viscosity η^{fR}, the inverse of the fluid's bulk modulus β^f and the fluid pressure in the fracture $\hat{p}$. Details concerning the derivation and the mentioned dimensional analysis of Eq. 4.2 could be obtained from the references mentioned e.g. in Schmidt (2022). The set of coupled partial differential equations in weak form for the poro-elastic domain and the embedded fractures could be implemented into a Finite Element framework, e.g. within software packages mentioned in the introduction.

4.1.1 Stiffness of Fractures

The change of deformation of a fracture does not only depend on the fluid pressure transients $\hat{p}(\hat{\mathbf{x}}, t)$. The local deformation of the fracture is also affected by local contact forces between asperities of the solid surfaces. In case of natural fractures which have always rough fracture surfaces, those contact forces could for instance occur in the case of "mechanically closed" but still "hydraulically open" fractures. In the present lower-dimensional modelling approach, the corresponding effective fracture stiffness caused by local contact forces could be taken into account and expressed with the contact related normal stresses (Bandis et al. 1983)

$$\sigma_N^{\text{con}} = E^{\text{Fr}} \frac{1}{\delta^c_{\text{max}} - \delta^c} \delta^c. \tag{4.3}$$

Note, that in Eq. 4.3 we considered only normal stresses, i.e. stress components normal to the fracture plane. Shear stresses within the fracture surface are neglected a priori. In the most simple linear constitutive approach, the effective contact normal stresses are proportional to the change of aperture described with the fracture closure δ^c and the maximum fracture closure δ^c_{max}, cf. Gens et al. (1990) and results in Fig. 4.2 . In this linear constitutive relation we have introduced, as an inherent material parameter of the contact law, an effective normal stiffness E^{Fr}.

On the laboratory scale, the introduced effective stiffness parameter could be determined in well-defined experiments. Therefore, natural fractures, obtained from mode 1 hydraulic fracture experiments, are mechanically tested, e.g. under harmonic excitation, cf. Fig. 4.3.

4.1.2 Strong Versus Weak Coupling

Implementation of the coupled set of partial differential equations introduced in terms of the biphasic poro-elastic and hybrid-dimensional flow model (Eqs. 4.1 and 4.2) might be distinguished regarding the chosen coupling scheme. In terms of the numerical strategy to reach equilibrium, chosen numerical coupling schemes are distinguished, cf. Fig. 4.4. Here, we may distinguish between staggered and

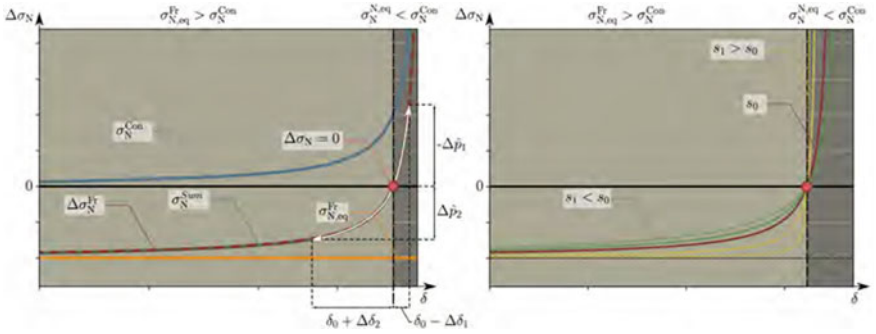

Fig. 4.2 Left: Relative normal stress changes as a function of the effective fracture aperture. Normal stress changes are expressed relative to the acting normal equilibrium stress state which is equivalent to the sum of induced contact forces and the constant equilibrium normal stress state. Effective aperture fluctuations are induced by perturbations of the equilibrium state by means of fluid pressure changes or vice versa. Right: Consideration of the fracture's microstructure in terms of a contact factor, respectively controlling the difference between initial hydraulic and mechanical opening

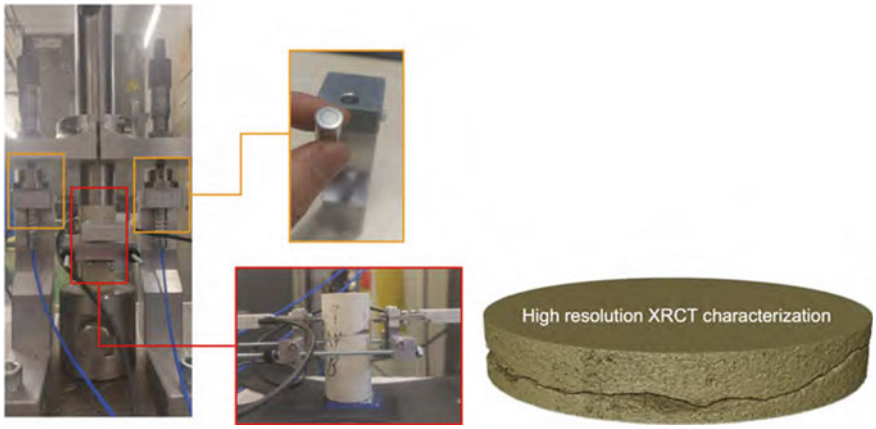

Fig. 4.3 Uniaxial setup for the determination of fracture stiffness E^{Fr} under harmonic excitation at different amplitudes in combination with fracture roughness characterization through high-resolution XRCT

monolithic approaches (Schmidt and Steeb 2019). Staggered numerical schemes treat the fracture and the rock bulk domain individually choosing solvers for both parts independently. Thus, highly efficient solvers for poro-elastic equations and for pressure diffusion equations could be adopted. This is especially interesting if large problems need to be solved, e.g. on HPC platforms (Schmidt et al. 2022b). Communication between the fracture domain $\mathcal{B}^{Fr}$ and the the rock domain $\mathcal{B}^{Pe}$ is conducted via boundary conditions, e.g. through special software packages like preCICE. Constraints have to be introduced in order to guarantee numerical stability.

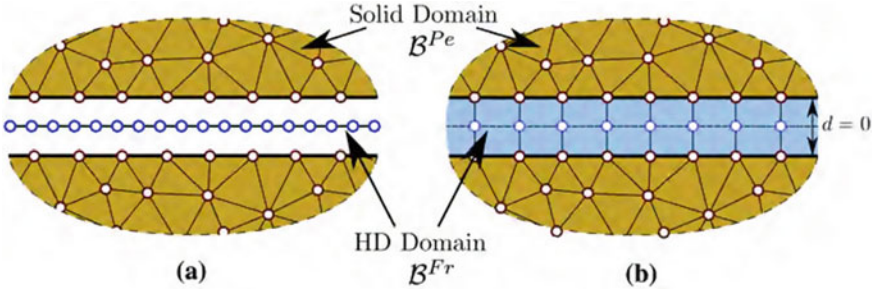

Fig. 4.4 Comparison of the weak coupling approach using non-conformal meshes (**a**) and a strong coupling approach with implemented interface elements (interface elements, and auxiliary nodes are explicitly shown for presentation purposes only; in the final discretization, the fracture surfaces align with $d = 0$) (**b**). Figure from Schmidt and Steeb (2019)

In contrast, monolithic coupling approaches build a single algebraic set of equations which is solved for both domains simultaneously.

Monolithic coupling of the fracture and the poro-elastic domain requires a mathematical discussion of the balance equations introduced to govern hydro-mechanical flow processes within the fracture, cf. Schmidt (2022), Schmidt and Steeb (2019).

4.2 Lower-Dimensional Representation of Frictional Interfaces

For constructing the weak form of the quasi-static equilibrium conditions

$$\operatorname{div} \boldsymbol{\sigma} + \varrho \mathbf{g} = \mathbf{0} \tag{4.4}$$

in the presence of displacement jumps we introduce an enriched test function $\mathbf{v}$ consisting of a continuous (standard) part $\mathbf{v}_c$ and a Heaviside enrichment $H(\mathbf{x})\mathbf{a}_\Gamma$ in the form

$$\mathbf{v} = \mathbf{v}_c + H(\mathbf{x})\mathbf{a}_\Gamma \tag{4.5}$$

with

$$H(\mathbf{x}) = \begin{cases} -0.5 & \forall \mathbf{x} \in \Omega^- \\ 0.5 & \forall \mathbf{x} \in \Omega^+ \end{cases} \tag{4.6}$$

Therefore, $(\mathbf{v}^+ - \mathbf{v}^-)_{\mathbf{x}_\Gamma} = [\![\mathbf{v}]\!]_\Gamma = \mathbf{a}_\Gamma$ represents the jump in the test function across the embedded discontinuity surface Γ. Superscripts $+$ and $-$ denote the opposite sides of the discontinuity surface. Then, we find the gradient of the test function as

$$\operatorname{grad} \mathbf{v} = \operatorname{grad} \mathbf{v}_c + \delta_\Gamma(\mathbf{x})[\![\mathbf{v}]\!]_\Gamma \otimes \mathbf{n}^- \tag{4.7}$$

where the Dirac function is defined and normalized as

$$\delta_\Gamma(\mathbf{x}) = \begin{cases} 0 & \forall \mathbf{x} \notin \Gamma \\ \infty & \forall \mathbf{x} \in \Gamma \end{cases} \quad \text{with} \quad \int_\Omega \delta_\Gamma(\mathbf{x})\, \mathrm{d}\Omega = 1 \tag{4.8}$$

To construct the weak form of Eq. (4.4)

$$0 = \int_\Omega \mathbf{v} \cdot \left[\operatorname{div} \boldsymbol{\sigma} + \varrho \mathbf{g} \right] \mathrm{d}\Omega \tag{4.9}$$

we perform partial integration of the stress divergence term by employing

$$\operatorname{div} \boldsymbol{\sigma} \cdot \mathbf{v} = \operatorname{div} (\boldsymbol{\sigma} \mathbf{v}) - \boldsymbol{\sigma} : \operatorname{grad} \mathbf{v}_\mathrm{c} - \boldsymbol{\sigma} : \delta_\Gamma(\mathbf{x}) [\![\mathbf{v}]\!]_\Gamma \otimes \mathbf{n}^- \tag{4.10}$$

which results in

$$\int_{\Omega \setminus \Gamma} \left[\boldsymbol{\sigma} : \operatorname{grad} \mathbf{v} - \varrho \mathbf{b} \cdot \mathbf{v} \right] \mathrm{d}\Omega + \int_\Gamma \boldsymbol{\sigma} \mathbf{n}^- \cdot [\![\mathbf{v}]\!]_\Gamma \, \mathrm{d}\Gamma = \int_{\partial\Omega} \bar{\mathbf{t}} \cdot \mathbf{v} \, \mathrm{d}\Gamma \tag{4.11}$$

With $\boldsymbol{\sigma} \mathbf{n}^- = \mathbf{t}^-$ and $\mathbf{t}^+ = \mathbf{t}_\Gamma = -\mathbf{t}^-$ we obtain

$$\int_{\Omega \setminus \Gamma} \left[\boldsymbol{\sigma} : \operatorname{grad} \mathbf{v} - \varrho \mathbf{b} \cdot \mathbf{v} \right] \mathrm{d}\Omega - \int_\Gamma \mathbf{t}_\Gamma \cdot [\![\mathbf{v}]\!]_\Gamma \, \mathrm{d}\Gamma = \int_{\partial\Omega} \bar{\mathbf{t}} \cdot \mathbf{v} \, \mathrm{d}\Gamma \tag{4.12}$$

Note that $\boldsymbol{\sigma}$ and $\mathbf{t}_\Gamma$ are the total stresses in a HM formulation of a fluid-saturated porous medium and thus couple into the following flow equations by means of the effective stress principle:

$$\boldsymbol{\sigma} = \boldsymbol{\sigma}' - \alpha_\mathrm{B} p \mathbf{I} \tag{4.13}$$

$$\mathbf{t}_\Gamma = \mathbf{t}'_\Gamma - \alpha_\mathrm{B}^\mathrm{f} p \mathbf{n}_\Gamma \tag{4.14}$$

Note also that the present work assumes continuity of the pressure between matrix and fracture ($p^\mathrm{m} \equiv p^\mathrm{f} \equiv p$).

In the above $\boldsymbol{\sigma}'$ is the effective stress tensor in the matrix, α_B and $\alpha_\mathrm{B}^\mathrm{f}$ are coefficients weighting the pore-pressure contribution in the matrix and fracture to be defined suitably, p is the fluid pressure, $\mathbf{I}$ is the identity tensor, $\varrho = \phi \varrho_\mathrm{FR} + (1 - \phi) \varrho_\mathrm{SR}$ is the bulk density of the porous medium comprising the densities of the liquid and the solid, ϱ_LR and ϱ_SR respectively, of porosity ϕ and $\mathbf{g}$ is the gravitational acceleration. In the fracture with local unit normal $\mathbf{n}_\Gamma$, $\mathbf{t}'_\Gamma$ represents the effective stress vector.

The effective quantities have to be supplied by constitutive equations. For the matrix, they are here given in incremental form

$$\mathrm{d}\boldsymbol{\sigma}' = \boldsymbol{\mathcal{C}}^\mathrm{m} : \mathrm{d}\boldsymbol{\epsilon}^\mathrm{e} \,, \tag{4.15}$$

where $\mathcal{C}^{\mathrm{m}}$ is the material stiffness tensor, $\boldsymbol{\epsilon} = \frac{1}{2}\left(\operatorname{grad}\mathbf{u} + \operatorname{grad}^{\mathrm{T}}\mathbf{u}\right)$ is the linear strain tensor, $\boldsymbol{\epsilon}^{\mathrm{e}}$ its elastic part and $\mathbf{u}$ is the solid displacement vector.

For the fracture effective stress, a connection is made constitutively to the displacement jump. Similar to the test function we specify $\mathbf{u} = \mathbf{u}_{\mathrm{c}} + H(\mathbf{x})\mathbf{w}(\mathbf{x}_\Gamma)$ such that $(\mathbf{u}^+ - \mathbf{u}^-)_{\mathbf{x}_\Gamma} = [\![\mathbf{u}]\!]_\Gamma = \mathbf{w}$. Then, in analogy to the incremental relationship for the matrix effective stress tensor, the fracture effective traction vector follows incrementally from elastic increments in the fracture face relative displacement vector

$$\mathrm{d}\mathbf{t}'_\Gamma = \mathbf{K}^{\mathrm{f}}\mathrm{d}\mathbf{w}^{\mathrm{e}} \tag{4.16}$$

where $\mathrm{d}\mathbf{w}^{\mathrm{e}}$ is the elastic part of the fracture relative displacement increment and $\mathbf{K}^{\mathrm{f}}$ is the second-order stiffness tensor of the fracture comprising normal and shear components.

For the following examples, the interface failure behaviour is of particular interest. Here, a Coulomb-type frictional interface was chosen

$$\mathrm{d}\mathbf{t}' = \mathbf{K}\mathrm{d}[\![\mathbf{u}]\!] = [K_{\mathrm{n}}(\mathbf{n}_\Gamma \otimes \mathbf{n}_\Gamma) + K_{\mathrm{s}}(\mathbf{I} - \mathbf{n}_\Gamma \otimes \mathbf{n}_\Gamma)]\,\mathrm{d}\mathbf{w}^{\mathrm{e}} \tag{4.17}$$

with a split of the displacement jump analogous to the strain split used in elasto-plasticity $\mathbf{w} = \mathbf{w}^{\mathrm{e}} + \mathbf{w}^{\mathrm{p}}$.

Based on the work by *Coulomb* in 1773 (Davis and Selvadurai 2002), the frictional failure criterion can be written as

$$\tau_{\mathrm{f}} = c - \sigma'_{\mathrm{n}} \tan\varphi \tag{4.18}$$

and describes a linear relationship between the limiting shear stress τ_{f} in a plane and the normal effective stress σ'_{n} (tension positive) acting on that plane based on the cohesion c and friction angle φ of the fracture. The plane is in our case given by the fracture plane and a yield function f_{y} describing the failure surface can be defined as follows

$$f_{\mathrm{y}} = \tau - c + \sigma'_{\mathrm{n}} \tan\varphi. \tag{4.19}$$

where τ is the acting shear stress in the fracture plane. For all states of stresses, which are within this envelope, i.e. $f_{\mathrm{y}} < 0$, no failure is predicted. This region grows as the fracture normal stress increases. Once $f_{\mathrm{y}} = 0$ is reached the fracture deformes plastically according to the flow rule

$$\mathrm{d}\mathbf{w}^{\mathrm{p}} = \mathrm{d}\lambda \frac{\partial g_{\mathrm{y}}}{\partial \mathbf{t}'} \tag{4.20}$$

where the plastic potential is formulated to allow for non-associated flow:

$$g_{\mathrm{y}} = \tau + \sigma'_{\mathrm{n}} \tan\psi. \tag{4.21}$$

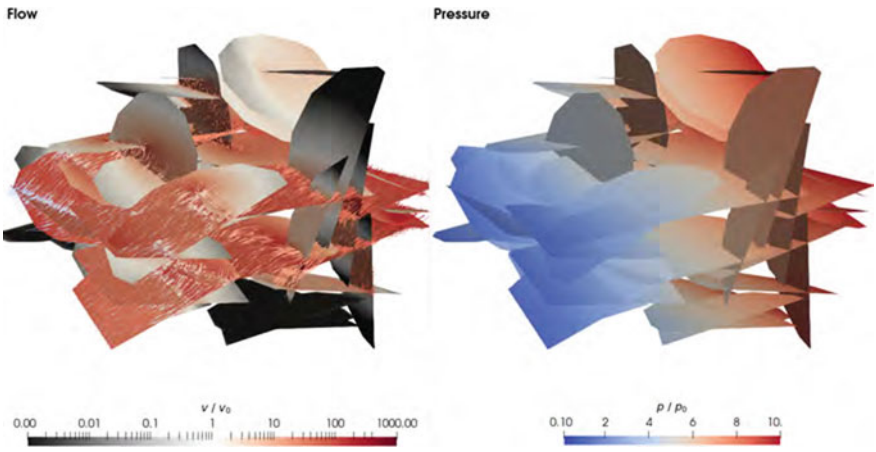

Fig. 4.5 Flow through discrete fracture network, where fractures are represented as 2D elements in a 3D setting (Lee 2022). Barsch & Nagel. Technische Universtität Bergakademie Freiberg. CC BY SA

where ψ is the dilatancy angle. Furthermore, the Kuhn-Tucker complementary conditions hold

$$f_y \lambda = 0 \qquad \lambda \geq 0 \qquad f_y \leq 0 \tag{4.22}$$

From the implicit integration of the material model the consistent stiffness matrix is passed back to the finite element assembly routines.

4.3 Verification and Application Examples

The lower-dimensional interface approach can be used to simulate flow in fracture networks. An example from OGS simulations is shown in Fig. 4.5.

In this chapter, however, examples for mechanical and hydromechanical effects will be described briefly.

4.3.1 Coulomb Model Verification

To test the functionality of the Coulomb implementation, a compressive stress is created by compressing an element assembly separated by an interface vertically by a tenth of the initial fracture aperture, i.e. by 1 µm, in a displacement-controlled manner. The top element is then sheared horizontally into the positive x direction by 10 µm, followed by shear unloading and reloading into the negative x direction by 10 µm, while the vertical displacement is held constant. The latter boundary condition

together with a positive dilatancy angle has the effect of increasing the fracture normal stress (accumulation of plastic normal fracture opening). Note that during this test the bottom boundary is fixed by a zero-displacement boundary condition whereas the boundaries at the left and right are freely movable.

Shearing causes a linear deformation in the horizontal direction until the applied shear exceeds the yield strength of the material. After this point, the shear stress increases at a lower rate until $u_x|_{y=2\mathrm{m}}$ reaches its maximum at maximum displacement, which illustrates the apparent hardening during the elasto-plastic deformation process under increasing confinement associated with the dilatant material response. Note that the material itself is not hardening but ideally plastic. Afterwards, the unloading /reloading due to shear reduces the shear stress in the same linear fashion observed in the initial stage of shearing (elastic unloading). After exceeding the yield strength, the material follows the dilatancy-induced apparent hardening again until maximum load reversal. The transition from linear deformation to material hardening after exceeding the yield strength clearly illustrates the effect of the Coulomb model on the overall deformation process. Also, the correct loading-unloading behaviour could be shown.

4.3.2 Soil-Structure Interfaces

Soil structure interactions play an important role in geotechnics. They include earth pressure development behind rough retaining walls, foundation tractions, interactions between tunnel liners and rock masses, driven piles, and many others.

Here, a simple laboratory test is chosen for illustrative purposes. Oedometer tests are a fundamental means of material characterization in geotechnical engineering. If the oedometer ring is compliant enough, radial stresses can be inferred in addition to the axial load in what is often called a soft oedometer. This example illustrates how the LIE model can be used to allow for relative displacement between the soil sample and the deformable walls of the soft oedometer.

The soft oedometer setup consists of two domains. The larger one represents the soil sample and the smaller one the compliant metal ring of the oedometer. The top boundary is assigned a constant normal traction representing the applied load. The bottom of the oedometer is fixed in the vertical direction and free to move in horizontal direction. The top and the right side of the metal ring are defined as traction free.

Due the Coulomb criterion, the soil can slide along the metal ring of the oedometer with a constant friction angle. Here, however, a frictionless interface was modelled. As illustration of the displacement discontinuity is the objective, the geomaterial is represented crudely oversimplified by a linear elastic model. The material properties of the benchmark are listed in the following table (Table 4.1):

Under the action of the top load, the soil gets compacted vertically (Fig. 4.6). The metal ring on the other hand experiences nearly no vertical displacements. The displacement jump in the solution is clearly visible by the transition from the smooth

Table 4.1 Material properties

Young's modulus of soil E_1	150 MPa
Young's modulus of metal ring E_2	210 GPa
Poisson's ratio of soil ν_1	0.2
Poisson's ratio of metal ring ν_2	0.3
normal stiffness of the fissure K_n	1×10^{15} Pa/m
shear stiffness of the fissure K_s	0 Pa/m
Top load p	1 MPa

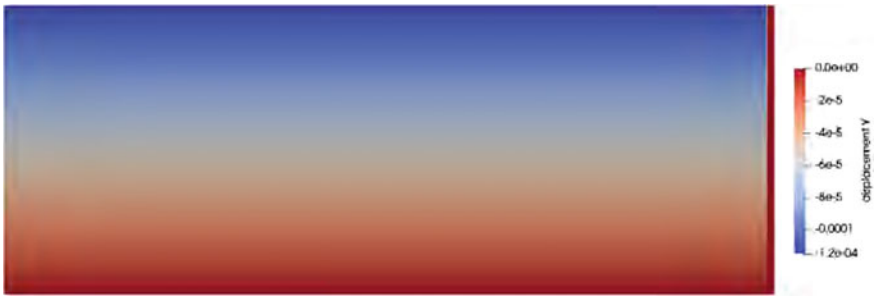

Fig. 4.6 Vertical displacements in the soft oedometer (OGS simulation). The use of frictional lower-dimensional elements allows for the establishment of a vertical displacement jump between the soil (smooth color gradient, left) and the oedometer ring (red zone with zero vertical displacements, right) in the solution on a single domain

color gradient to the red outer part of the domain. This jump is inherent in the finite elements pace due to the Heaviside enrichment described above.

For the chosen parameters and numerical settings, the radial displacements causing the expansion of the ring used for radial stress measurements reach about 5.5 µm at the circumference and cause radial stresses of around 0.229 MPa. This value is slightly lower than the 0.25 MPa that would be expected for a rigid ring. Likewise, the axial compaction of the sample itself is somewhat larger than in the case of a rigid ring. The exact values can be confirmed analytically by solving the linear elastic equilibrium problem for the sample subject to the top load boundary condition in conjunction with the pressure vessel equation, where both domains are connected via radial stress and displacement continuity.

4.3.3 Fault Slip Experiment (Mont Terri)

Simulations related to the FS experiment in Mont Terri (Guglielmi et al. 2017) are described elsewhere (Rutqvist et al. 2020). Here, we show more recent results

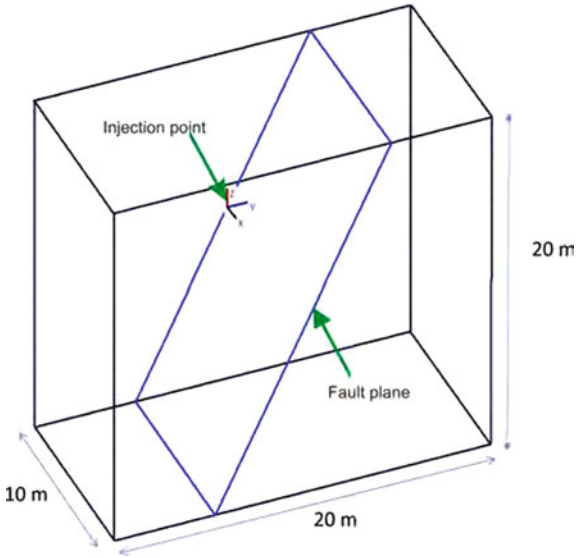

Fig. 4.7 3D model geometry for calculation of injection induced fault activation

using the LIE implementation described above. This example also links methods and application settings of WPs 2 and 3.

To simulate the fault slip displacement induced by fluid injection-induced overpressures, we define a 3D model domain (Fig. 4.7), which broadly represents the minor fault geometry embedded in the rock matrix (Rutqvist et al. 2020). The model domain has edge lengths of 20 m and contains the fault dipping at 65°. Symmetry in the x direction is assumed and used to reduce the computational effort, therefore the side-length in the x direction reduces to 10 m.

The host rock matrix is modelled using linear elasticity assuming an isotropic material behavior with a bulk modulus of 5.9 GPa and a shear modulus of 2.3 GPa, based on the average values derived from experiments on Opalinus Clay at Mont Terri. For all outer boundaries of the matrix we assume roller boundary conditions. Based on a simplified experimental data set, the in-situ stress field is characterized by $\sigma_{zz} = -7$ MPa ,$\sigma_{yy} = -6$ MPa $\sigma_{xx} = -3.3$ MPa, where negative values indicate compression. Hydraulically, the host rock is considered impermeable because of the very low permeability of Opalinus Clay and the relatively short time-frame of these experiments. Fracture flow with various permeability models (constant, cubic law, cubic law only after shear slip, etc.) is applied while the fracture is assigned Coulomb behaviour. In this hydraulic-mechanical approach, a sudden increase in hydraulic aperture by a pre-set factor is modelled once shear failure occurs (Rutqvist et al. 2020). After fault activation, further aperture changes due to hydraulic-mechanical coupling are calculated by the cubic law. To parameterize the fluid phase and the porous medium we use standard values, see Table 4.2.

The initial fluid pressure estimated from site measurements was set to 0.5 MPa while the effective fracture traction is calculated from the stress field in the matrix

Table 4.2 Material properties for the modelling scenarios of the fault-slip experiment, scenario 1

Material	Parameter	Value
		Scenario Nr.
Fault	Normal stiffness K_n [GPa/m]	20
	Shear stiffness K_s [GPa/m]	20
	Static friction angle [°]	22
	Tensile strength [MPa]	0
	Permeability model	Cubic law after slip
Host rock matrix	Bulk modulus K [GPa]	5.9
	Shear modulus G [GPa]	2.3
	Bulk density ϱ [kg/m^3]	2450
	Permeability [m^2]	0
Fluid	Density ϱ [kg/m^3]	1000
	Compressibility [Pa^{-1}]	4.4e-9
	Dynamic viscosity μ [Pa s]	1.0e-3

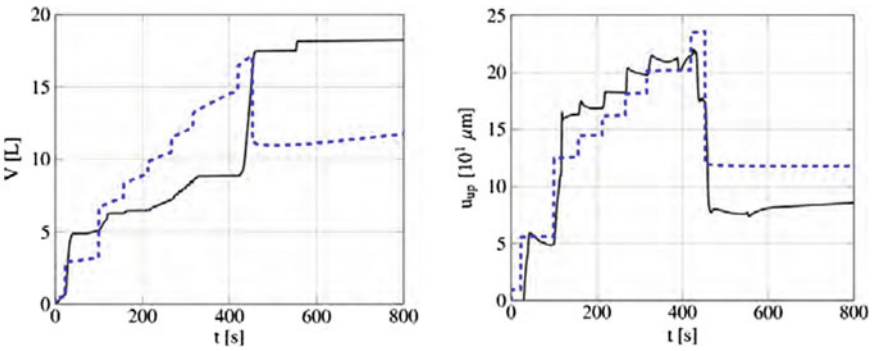

Fig. 4.8 Injection volume and fracture aperture change (numerical and experimental) using fully-coupled LIE models driven by step-wise injection pressure increases

by appropriate tensor rotation operations. The pressure and stress fields are assumed to be uniform and we neglect gravity in this case.

An initial comparison between the results of the numerical calculation and the laboratory data still shows an offset in the results (Fig. 4.8). Currently, parameter studies on the initial stress field, the hydraulic and mechanical fault properties, the activation mechanism and the injection control are undertaken to improve the results. Other modelling approaches were published in an overview paper (Rutqvist et al. 2020). Another modelling approach implemented in OGS was published in Urpi et al. (2020). These references contain details on the hydraulic models and the interpretation of the experimental data. A publication based on the approach presented here is currently under preparation.

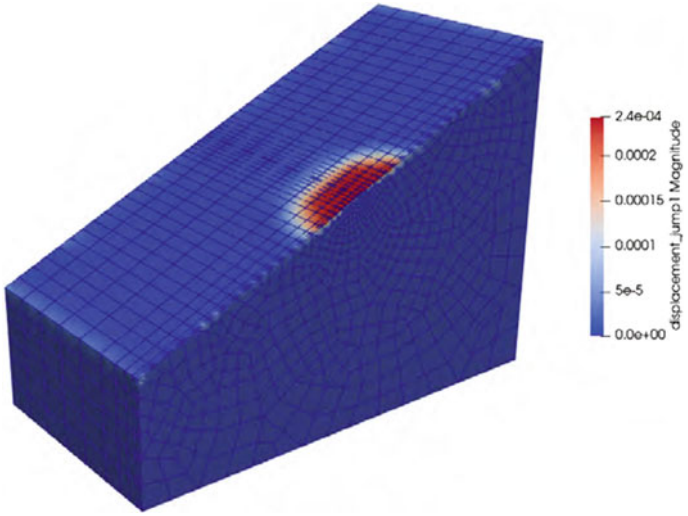

Fig. 4.9 Area of fault affected by shear slip

The area affected by shear slip, in which the fault transmissibility is drastically changed due to fault activation, is highlighted in Fig. 4.9. The area is centered around the injection point and is roughly circular in shape. This is inline with other modelling studies (Rutqvist et al. 2020).

4.4 Concluding Remarks

Lower-dimensional continua are mechanically and numerically intricate ways of representing interfaces of various kinds, including contact zones, fractures, faults, etc. Conceptually, the co-dimensional entities are generated by integration in their normal direction while making specific assumptions on the distribution of certain field quantities in this direction. Numerically, they can be represented by enrichment of finite element spaces and interface elements, for example. This kind of representation comes with both advantages and disadvantages compared to other methods. While this chapter showed examples on hydraulic, mechanical and hydromechanical behaviour of elastic and frictional interfaces, further aspects related to fracture mechanics and hydraulic fracturing are discussed in Yoshioka et al. (2019), Mollaali et al. (2022).

References

Bandis, S., Lumsden, A., & Barton, N. (1983). Fundamentals of rock joint deformation. *International Journal of Rock Mechanics and Mining Sciences & Geomechanics Abstracts, 20,* 249–268.

Biot, M. A. (1941). General theory of three-dimensional consolidation. *Journal of Applied Physics, 12*(2), 155–164.

Davis, R. O., & Selvadurai, A. P. S. (2002). *Plasticity and geomechanics*. Cambridge: Cambridge University Press.

Gens, A., Carol, I., & Alonso, E. (1990). A constitutive model for rock joints formulation and numerical implementation. *Computers and Geotechnics, 9,* 3–20.

Guglielmi, Y., Birkholzer, J., Rutqvist, J., Jeanne, P., & Nussbaum, C. (2017). Can fault leakage occur before or without reactivation? Results from an in situ fault reactivation experiment at Mont Terri. *Energy Procedia, 114*, July 2017, 3167–3174.

Lee, H. (2022). Solving the rock-hard problem of nuclear waste disposal burial is best. *Ars Technica*, 1–11.

Mollaali, M., Kolditz, O., Mengsu, H., Park, C.-H., Park, J.-W., McDermott, C., Chittenden, N., Bond, A., Yoon, J., Zhou, J., Pan, P.-Z., Liu, H., Hou, W., Lei, H., Zhang, L., Nagel, T., Barsch, M., Wang, W., Nguyen, S., Kwon, S., Lee, C., & Yoshioka, K. (2022). Comparative verification of hydro-mechanical fracture behavior: Task g of international research project DECOVALEX 2023. *International Journal of Rock Mechanics and Mining Sciences* (under review).

Renner, J. (2020). STIMTEC: A mine-scale hydraulic stimulation experiment of anisotropic metamorphic rock with evaluation by mine-back drilling. ARMA Newsletter.

Rutqvist, J., Graupner, B., Guglielmi, Y., Kim, T., Maßmann, J., Nguyen, T. S., et al. (2020). An international model comparison study of controlled fault activation experiments in argillaceous claystone at the Mont Terri laboratory. *International Journal of Rock Mechanics and Mining Sciences, 136,* 104505.

Schmidt, P. (2022). *Hydro-mechanical coupling of flow in deformable high-aspect ratio fractures*. Ph.D. thesis, University of Stuttgart.

Schmidt, P., & Steeb, H. (2019). Numerical aspects of hydro-mechanical coupling of fluid-filled fractures using hybrid-dimensional element formulations and non-conformal meshes. *GEM - International Journal on Geomathematics, 10*(1), 1–36.

Schmidt, P., Steeb, H., & Renner, J. (2021). Investigations into the opening of fractures during hydraulic testing using a hybrid-dimensional flow formulation. *Environmental Earth Sciences, 80,* 497.

Schmidt, P., Dutler, N., & Steeb, H. (2022a). Importance of fracture deformation throughout hydraulic testing under in situ conditions. *Geophysical Journal International, 228,* 493–509.

Schmidt, P., Jaust, A., Steeb, H., & Schulte, M. (2022b). Simulation of flow in deformable fractures using a quasi-newton based partitioned coupling approach. *Computational Geosciences, 26,* 381–400.

Steeb, H., & Renner, J. (2019). Mechanics of poro-elastic media: A review with emphasis on foundational state variables. *Transport in Porous Media, 130*(2), 437–461.

Urpi, L., Graupner, B., Wang, W., Nagel, T., & Rinaldi, A. P. (2020). Hydro-mechanical fault reactivation modeling based on elasto-plasticity with embedded weakness planes. *Journal of Rock Mechanics and Geotechnical Engineering, 12*(4), 877–885.

Vinci, C., Renner, J., & Steeb, H. (2014). A hybrid-dimensional approach for an efficient numerical modeling of the hydro-mechanics of fracture. *Water Resources Research, 50,* 1616–1635.

Watanabe, N., Wang, W., Taron, J., Görke, U. J., & Kolditz, O. (2012). Lower-dimensional interface elements with local enrichment: Application to coupled hydro-mechanical problems in discretely fractured porous media. *International Journal for Numerical Methods in Engineering*, *90*(8), 1010–1034.

Yoshioka, K., Parisio, F., Naumov, D., Lu, R., Kolditz, O., & Nagel, T. (2019). Comparative verification of discrete and smeared numerical approaches for the simulation of hydraulic fracturing. *GEM - International Journal on Geomathematics, 10*(1), 13.